

Drift-wave-like density fluctuations in the Advanced Toroidal Facility (ATF) torsatron

M. G. Shats

Australian National University, Canberra, Australia

J. H. Harris, K. M. Likin,^{a)} J. B. Wilgen, L. R. Baylor, J. D. Bell,^{b)} C. H. Ma, M. Murakami, K. A. Sarkisyan,^{a)} S. C. Aceto,^{c)} T. S. Bigelow, G. L. Bell, R. J. Colchin, R. A. Dory, J. L. Dunlap, G. R. Dyer, A. C. England, R. C. Goldfinger,^{b)} G. R. Hanson, D. P. Hutchinson, R. C. Isler, T. C. Jernigan, R. A. Langley, D. K. Lee,^{b)} J. F. Lyon, A. L. Qualls, D. A. Rasmussen, R. K. Richards, M. J. Saltmarsh, J. E. Simpkins, K. L. Vander Sluis, and J. J. Zielinski^{d)}

Oak Ridge National Laboratory, Oak Ridge, Tennessee 37831-8072

(Received 14 February 1994; accepted 12 October 1994)

Density fluctuations in low-collisionality, low-beta ($\beta \sim 0.1\%$), currentless plasmas produced with electron cyclotron heating (ECH) in the Advanced Toroidal Facility (ATF) torsatron [Fusion Technol. **10**, 179 (1986)] have been studied using a 2 mm microwave scattering diagnostic. Pulsed gas puffing is used to produce transient steepening of the density profile from its typically flat shape; this leads to growth in the density fluctuations when the temperature and density gradients both point in the same direction in the confinement region. The wave number spectra of the fluctuations that appear during this perturbation have a maximum at higher $k_{\perp} \rho_s$ (~ 1) than is typically seen in tokamaks. The in-out asymmetry of the fluctuations along the major radius correlates with the distribution of confined trapped particles expected for the ATF magnetic field geometry. During the perturbation, the relative level of the density fluctuations in the confinement region (integrated over normalized minor radii ρ from 0.5 to 0.85) increases from $\tilde{n}/n \sim 1\%$ when the density profile is flat to $\tilde{n}/n \sim 3\%$ when the density profile is steepened. These observations are in qualitative agreement with theoretical expectations for helical dissipative trapped-electron modes (DTEMs), which are drift-wave instabilities associated with particle trapping in the helical stellarator field; they suggest that trapped-electron instabilities may play a role in constraining the shape of the density profile in ATF, but have little effect on global energy confinement. © 1995 American Institute of Physics.

I. INTRODUCTION

The radial transport of energy and particles in magnetically confined plasmas in tokamak and stellarator experiments is much larger than expected from fundamental neo-classical transport theory, and the search for an understanding of “anomalous” transport mechanisms continues to be a major component of contemporary controlled fusion research.^{1,2} Accordingly, considerable effort is being expended in studying the plasma fluctuations and turbulence that are the likely causes of enhanced radial transport. Since the magnitude and functional dependence of global energy confinement in tokamaks and stellarators appear to be quite similar, in spite of the rather different magnetic topologies and plasma stability properties of these devices, comparisons of fluctuation phenomena in these two confinement geometries can shed light on the physics underlying transport phenomena.

Instabilities associated with particles trapped in the magnetic mirrors produced by the geometry of the confining field

have been observed in linear experiments³ and have long been suspected to be important in toroidal confinement, since they can result in effective heat transport coefficients that increase with temperature in a fashion similar to that seen in some experiments.^{2,4} Recent advances in measurements of turbulence in hot tokamak plasmas⁵⁻⁷ are improving the knowledge of turbulence characteristics and their dependence on plasma parameters and heating. However, a clear picture of the role of trapped-particle instabilities in tokamak and stellarator experiments has yet to emerge.

In tokamaks, dissipative trapped-electron modes (DTEMs)⁸ are drift waves that are destabilized by the particle population trapped in the inhomogeneities of the magnetic field strength $|B|$ produced by the $1/R$ dependence of the toroidal magnetic field. In toroidal stellarators, the helical ripple in $|B|$ (which has relative amplitude ϵ_h) due to the stellarator field results in an additional particle trapping mechanism that can also lead to trapped-particle instabilities.⁹ Since the connection length of the helical field ripples $L_{\parallel h} \approx 2\pi R/M$ (where M is the number of stellarator field periods) is typically much shorter than the connection length of the toroidal magnetic well $L_{\parallel t} \approx qR$, the electron collisionality $\nu_h^* = \nu_{\text{eff}} L_{\parallel h} / V_{te}$ for helical trapping (here $\nu_{\text{eff}} = \nu_{ei} / \epsilon_h$ is the effective electron collision frequency and V_{te} is the electron thermal velocity) is proportionally lower than the toroidal collisionality ν_t^* at the same temperature and density. For the electrons, the condition $\nu_{eh}^* < 1$ required

^{a)}Permanent Address: General Physics Institute, Moscow, Russian Federation.

^{b)}Permanent Address: Computing and Telecommunications Division, Martin Marietta Energy Systems, Inc., Oak Ridge, Tennessee 37831-8072.

^{c)}Permanent Address: Interscience, Inc., Troy, New York 12181.

^{d)}Permanent Address: Rensselaer Polytechnic Institute, Troy, New York 12181.

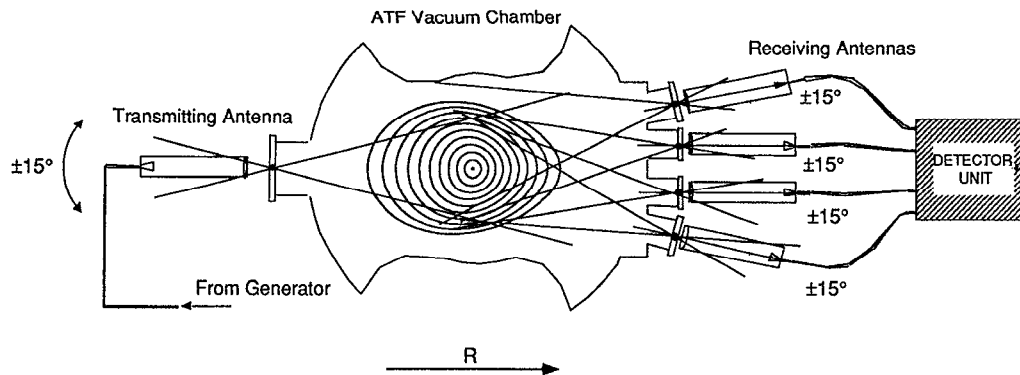


FIG. 1. Layout of the 2 mm scattering diagnostic on ATF.

for helical DTEMs can be fulfilled even at modest plasma parameters ($T_e \sim 1$ keV, $\bar{n}_e \leq 10^{13}$ cm $^{-3}$) like those achieved during operation with electron cyclotron heating (ECH) in present-day stellarators.

The Advanced Toroidal Facility¹⁰ (ATF) is well suited to studies of plasma turbulence and transport because of its capabilities for control of plasma parameters and magnetic configuration, as well as its variety of diagnostics designed to study local transport and fluctuations. A number of fluctuation diagnostics have already yielded valuable information on magnetic fluctuations¹¹ and potential fluctuations, both at the plasma edge [fast reciprocating Langmuir probe (FRLP)^{12,13}] and in the interior [heavy-ion beam probe (HIBP)¹⁴]. Density fluctuations have been studied using the FRLP, the HIBP, and correlation reflectometry.^{15,16} The microwave scattering diagnostic is an important addition to this set, because it permits measurements of wave number spectra in a broad k range and has access to the entire plasma cross section. The spatial resolution of the microwave scattering diagnostic is sufficient to distinguish among fluctuations in the plasma core, in the confinement region, and at the plasma edge. Thus, this diagnostic is extremely useful for the study of ECH plasmas in ATF, which are generally characterized by flat to hollow density profiles and comparatively low average densities ($\bar{n}_e \leq 10^{13}$ cm $^{-3}$).^{17,18} Plasmas in this regime are marginally stable to DTEMs in the core and dominated by pressure-gradient-driven resistive interchange modes at the edge.^{9,17,18} Pushing the plasma out of this marginally stable condition in some way could make it possible to observe the excitation of drift-wave-induced turbulence. These quiescent discharges have low normalized plasma pressure $\beta = p/(B^2/2\mu_0) \approx 0.1\%$, and only a small residual plasma bootstrap current¹⁹ of ~ 1 – 2 kA, so it is highly unlikely that competing pressure or current-driven MHD phenomena are involved in the fluctuations; this removes a significant degree of complication from these experiments.

In this paper we describe experiments that were specifically designed to look for evidence of trapped-electron instabilities. In Sec. II, we describe the ATF device, its diagnostics, and the experimental procedure. In Sec. III we describe the setup and calibration of the microwave scattering system. In Sec. IV we describe experiments in which gas puffing was

used to produce conditions that could be expected to excite trapped-electron instabilities. In Sec. V we describe turbulence measurements for a number of different magnetic configurations. In Sec. VI we compare the experimental results with theoretical expectations for trapped-electron drift-wave instabilities, and in Sec. VII we summarize the conclusions.

II. EXPERIMENTAL SETUP

ATF is a large stellarator-type device with a major radius $R_0 = 2.1$ m, average plasma radius $\bar{a} = 0.27$ m, and magnetic field $B \leq 1.9$ T. Its confining field and flux surfaces are produced by a torsatron helical winding set having poloidal multipolarity $l = 2$ and $M = 12$ toroidal field periods, and by associated poloidal field coils. In its nominal magnetic configuration, ATF has a central rotational transform $\iota_0 = 1/q_0 = 0.3$ and an edge rotational transform $\iota_a = 1/q_a \approx 1$. The helical magnetic field ripple is near zero on the magnetic axis and rises approximately proportional to ρ^2 to ≈ 0.3 at the plasma edge ($\rho = r/\bar{a}$ is the normalized plasma minor radius).

A four-channel, 2 mm microwave scattering system is used to study density fluctuations in ATF. (Details of the setup and calibration procedure for this diagnostic are given in Sec. III.) A steerable transmitting antenna is mounted in a port on the inside (small-major-radius side) of the torus, and four receiving antennas are mounted on outside ports. The scattering volume can be spatially scanned over the plasma minor cross section, as shown in Fig. 1. The diameter of the Gaussian microwave beams is 3.2 cm at the beam waist. The range of accessible fluctuation perpendicular wave numbers is 3 cm $^{-1} \leq k_\perp \leq 20$ cm $^{-1}$ and varies with the location of the scattering volume. The spatial resolution of the system varies with the scattering angle ($\theta_s \leq 40^\circ$) and with the location of the intersection of the incident and scattered microwave beams, but typically it is better for higher k_\perp (larger θ_s). In practice, to resolve the contributions to the scattered wave from the plasma core ($\rho < 0.5$), the confinement region ($0.5 \leq \rho \leq 0.85$), and the plasma edge ($\rho > 0.85$), only signals with $k_\perp > 6$ cm $^{-1}$ are used in the data analysis. When the scattering volume is located above or below the plasma center (i.e., at $R = R_0$), fluctuations with predominantly radial

wave numbers ($k_\rho \gg k_\theta$) scatter the incident beam. If the scattering volume is close to the equatorial plane of the torus ($z \approx 0$), fluctuations with predominantly poloidal wave numbers ($k_\theta \gg k_\rho$) contribute to the scattered beam.

A microwave generator with frequency $f = 135$ GHz and output power $P = 0.5$ W is used. The incident microwave beam polarization is chosen to be ordinary mode, i.e., the electric field (E_0) vector of the incident wave is parallel to the magnetic field on the magnetic axis. Homodyne and dual-homodyne²⁰ measurements (in the latter, a pair of quadrature detectors is used at each channel) are made to find the intensities and the propagation direction of the fluctuations. Four 12-bit, 130 kbyte digitizers, operating at a sampling frequency of 1 MHz, store two time samples (130 ms each) of each of the four detector signals during each ATF shot. The frequency of the digitizers allows analysis of the fluctuation frequency spectra up to 400 kHz; active four-pole low-pass filters are used to attenuate signals above this frequency to prevent aliasing.

The results are arranged in a database, which includes plasma-related parameters (e.g., average density, plasma stored energy, gyrotron power, and currents in the magnetic coils) along with spectral representations of the scattering signals determined from fast-Fourier transform (FFT) digital signal processing.²¹ The spectral data include the mean square values of the signals for each channel, calculated for six frequency bands in the range from 2 to 250 kHz, and the spectrally averaged frequencies of the signals. These quantities are calculated for 20 ms analysis intervals. Each interval is further subdivided into overlapping 512-point segments to produce 77 spectral realizations for the FFT processing. Another database documents antenna geometries, characteristics of the magnetic configurations, and the results of the scattering geometry analysis (location and dimensions of the scattering volume, average density in each scattering volume, number of electrons, spatial resolution, fluctuation wave numbers, etc.) for each ATF discharge. The scattering volume characteristics (the average density and the number of electrons in the scattering volume) and the analysis of the correlation of the density fluctuation intensity are based on measurements of the density profiles by a 15-channel far-infrared (FIR) interferometer.²² Electron temperature profiles are determined using an electron cyclotron emission diagnostic system.²³ The HIBP^{14,18} was used to measure radial profiles of plasma potential for selected data sequences.

III. SETUP AND CALIBRATION OF THE SCATTERING DIAGNOSTIC

Scattering measurements have the distinct advantage of yielding wave-number-resolved spectra of fluctuations. It is necessary, however, to make special provisions to obtain useful information about fluctuation amplitudes and the spatial localization of the measurements. In this section, we summarize the procedures used to accomplish this in the ATF scattering experiments. Since the details of the microwave beam optics and scattering geometry are important in these measurements, a detailed view of the scattering geometry used in these experiments is shown in Fig. 2 for reference.

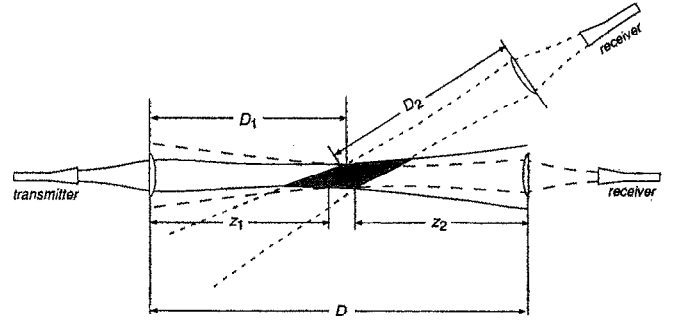


FIG. 2. Scattering geometry: D is the distance between the transmitter and the receiver during the calibration *in situ*; D_1 and D_2 are, respectively, the distances from the center of the scattering volume to the transmitting and receiving antennas; and z_1 and z_2 are the distances from the antennas to the waist of the microwave beam.

A. Determination of scattered power spectra

The microwave power scattered into the receiving antenna by the plasma density fluctuations is²⁴

$$P_S = I_0 r_e^2 \Omega N_e \int_{-\infty}^{\infty} S(k, \omega) d\omega / 2\pi, \quad (1)$$

where the classical electron radius $r_e = 2.8 \times 10^{-13}$ cm, I_0 is the time average of the Poynting vector of the incident wave, N_e is the number of electrons in the scattering volume, Ω is the solid angle of reception, and $S(k, \omega)$ is the spectral power density function of the fluctuations. In terms of microwave beam parameters, $I_0 = P_T / [4\pi w_T^2(z_{TS})]$ [where $w_T(z_{TS})$ is the half-width of the incident beam measured at the center of the scattering volume], and $\Omega = w_R^2(z_2) / D_2^2$ (where D_2 is the distance from the center of the scattering volume to the receiver). The scattered power defined in terms of beam parameters is then

$$P_S = P_T \frac{w_R^2(z_2)}{4\pi D_2^2 w_T^2(z_{TS})} r_e^2 N_e \int_{-\infty}^{+\infty} S(k, \omega) d\omega. \quad (2)$$

To determine the fluctuation spectral power density $S(k, \omega)$, we need to know the ratio of the scattered to the incident power P_S / P_T , the scattering geometry parameters (the distances D_2 , z_2 , and z_{TS}), the widths of the microwave beams, and the number of electrons in the scattering volume N_e .

We measure P_T at the transmitting antenna. When the transmitting and receiving antennas are aligned so as to face each other, we measure the ratio of the microwave power at the detector P_R to the incident power P_T . This ratio includes power losses due to the power transmission from one antenna to another (directivity loss) and losses in the transmission line and microwave circuit elements:

$$P_R = P_T k_l \left[1 - \exp\left(-\frac{2w_R^2(z_2)}{w_T^2(D-z_1)}\right) \right] = P_T k_l k_g, \quad (3)$$

where $w_T(D-z_1)$ is the half-width of the transmitter beam measured at the position of the lens of the receiver, k_l is the waveguide loss coefficient, and k_g is the directivity loss. Using a square-law detector that has a sensitivity of A , we

determine the power losses in the waveguide to be $k_l = U_R/(U_T k_g)$, where U_R and U_T are the responses of the detector to the received and transmitted power correspondingly. If this detector is used in the homodyne scheme for the measurements of the scattered power P_S , its response also depends on the microwave power in the reference channel (local oscillator power) P_{ref} : $U_{Sd} = A \sqrt{P_{Sd} P_{\text{ref}}}$, where $P_{Sd} = k_l P_S$. In other words,

$$\frac{P_S}{P_T} = \frac{\langle U_{Sd}^2 \rangle}{k_l U_T U_{\text{ref}}},$$

where the angle brackets denote the time averaging of the detector signal. Using Eq. (3) in Eq. (2), we finally arrive at

$$S(k) = \frac{\langle U_{Sd}^2 \rangle}{U_R U_{\text{ref}}} k_g \frac{4 \pi D_2^2 w_T^2(z_{TS})}{w_R^2(z_2)} (r_e^2 N_e)^{-1}, \quad (4)$$

which uses both measured (U_R , U_{ref} , U_{Sd} , k_g) and computed [D_2 , $w_T(z_{TS})$, $w_R(z_2)$, N_e] quantities.

The microwave beam parameters were experimentally determined using a test stand built to the exact dimensions of the ATF chamber cross section before the diagnostic was installed on ATF itself. The microwave beam waist was measured as a function of distance from the antenna and was found to agree to within 2% with the optics calculations. Therefore, we use these “semimeasured” values of w_T and w_R in the spectral power density computations in Eq. (4). This leaves the number of electrons inside the scattering volume N_e to be determined for experimental density profiles in the actual magnetic confinement geometry.

The location of the scattering volumes in the magnetic flux surface geometry can be determined accurately because of the special circumstance of this series of stellarator experiments. Since the plasma pressure is very low for these experiments ($\beta \approx 0.1\%$), the magnetic geometry is negligibly different from that of the vacuum magnetic surfaces, which are determined from the external coil currents. The microwave beam propagation ($f = 135$ GHz) is also essentially unaffected by the presence of this low-density plasma: ray tracing calculations with the RAYS three-dimensional ray tracing code²⁵ (which incorporates the full stellarator field) showed that refraction of the microwave beam is negligible at the low densities of $(5-10) \times 10^{12} \text{ cm}^{-3}$ used in these experiments.

The scattering volumes are determined as an intersection of two cylinders at the scattering angle θ_s defined by the Bragg condition. Then, a Monte Carlo code is used to determine the total number of electrons inside the scattering volume, using as inputs the experimental density profiles (from HCN interferometer measurements²²), the computed magnetic surfaces (from the VMEC code²⁶), the angles of the transmitting and the receiving antennas, and the microwave beam parameters. The outputs of the code are the radial location of the scattering volume ρ_{min} , ρ_{max} , the fluctuation wave number k_{\perp} and its components k_{ρ} , k_{θ} (resolved in the magnetic surface geometry), the number of electrons in the scattering volume N_e , and an average density in the scattering volume,

$$\bar{n}_S = \int_{V_S} n \, dV / V_S.$$

This information is stored in the database files for a number of magnetic configurations and is used for analysis of the wave number spectra and the calculations of the relative fluctuation level.

After the scattering system was set up on ATF, we verified that when the scattering volume was positioned inside the plasma, the spectral power density measured by the receiving antennas was a factor of 10–100 higher than was the case when the scattering volume was located outside the plasma. This indicated at a basic experimental level that indirect scattering from the walls, etc., was not contaminating the scattering measurements.²⁷

B. Determination of fluctuation levels

Using the definition of the spectral power density,

$$S(k, \omega) = \frac{1}{V_S T} \frac{\langle |\tilde{n}(k, \omega)|^2 \rangle_{V_S T}}{\bar{n}_S}, \quad (5)$$

the density fluctuation level can be calculated from experimental measurements of $S(k, \omega)$ as

$$\langle |\tilde{n}|^2 \rangle = \frac{\bar{n}_S}{(2\pi)^4} \int \int S(k, \omega) dk d\omega. \quad (6)$$

The smallest parallel wavelength that is likely to be present in ATF is given by the toroidal scale length of the helical stellarator field $L_{\parallel} = 2\pi R/M$ (here $M = 12$ is the number of field periods). This parallel wavelength corresponds to $k_{\parallel} = 0.06 \text{ cm}^{-1}$, which is much smaller than any perpendicular wave number k_{\perp} in the present experiment. Thus, following the approach used on the Tokamak Fontenay aux Roses (TFR),²⁸ we estimate the contribution of the fluctuation parallel wavelength to be of the order π/w_{\parallel} , where w_{\parallel} is the minimum of the microwave beam widths w_T and w_R in the center of the scattering volume.

If we assume symmetry of the density fluctuation spectrum in the poloidal plane (suggested by the experimental results in tokamaks), the fluctuation level can be determined as

$$\langle |\tilde{n}|^2 \rangle = \frac{\bar{n}_S}{8\pi^2 w_{\parallel}} \int_{k_{\perp}} S(k_{\perp}) k_{\perp} dk_{\perp}. \quad (7)$$

Here we have assumed the density fluctuation spectrum to be in the plane perpendicular to **B**.

In the actual experiment, the poloidal plane of measurements deviates from the plane perpendicular to the magnetic field by the value of the pitch angle. In ATF, the field line pitch angle ($\tan^{-1} \alpha$) varies significantly within the confinement volume because of the stellarator field. In the plasma cross section where the scattering measurements are made, the tangent of the pitch angle can be represented in terms of geometrical parameters with the expression²⁹

$$\alpha = \left(\frac{B_{\theta}}{B_T} \right) = \frac{\epsilon_{h0} \rho \cos 2\theta}{\gamma(1 - \epsilon_{h0} \rho^2 \cos 2\theta - \epsilon_{i0} \rho \cos \theta)}. \quad (8)$$

Here B_θ and B_T are the spatially varying poloidal and toroidal magnetic field components, respectively; θ is the poloidal angle measured from the midplane on the large R side of the torus; $\gamma = Ma_c/IR_0$ is the pitch parameter of the external stellarator field, with a_c the minor radius of the helical coil set; ϵ_{h0} and ϵ_{t0} are, respectively, the helical field ripple and the toroidal field variation (=the inverse aspect ratio, a/R). For the ATF configuration used in this experiment, $a_c = 0.48$ m, $\gamma = 1.37$, $\epsilon_{h0} = 0.35$, and $\epsilon_{t0} = 0.14$. For the most important scattering volumes used in this study (see Sec. IV A), the pitch angles at the reference radius of $\rho = 0.6$ are $\tan^{-1}\alpha \approx 5^\circ - 6^\circ$.

Because of the nonuniform helical field and the variety of scattering volumes used in these experiments, there are scattering contributions from plasma waves with finite k_\parallel that can project into the various k_\perp channels. However, as noted earlier, the largest likely value of k_\parallel is $\sim 0.06 \text{ cm}^{-1}$, so that the projection of k_\parallel into the k_\perp channels by virtue of field line tilt is even less than this value.

There is also a “false” k_\parallel scattering component produced by the projection of k_\perp due to the finite pitch angle. For the scattering volumes of interest in this study, this component has an apparent $k_\parallel \approx \alpha k_\perp = 0.12 k_\perp$, and can be neglected.

A more significant effect of the finite field line pitch on scattering spectra has been pointed out by Truc *et al.*³⁰ and Holzauer *et al.*³¹ Because of the finite extent of the scattering volume along the field line (limited by the radii of the Gaussian beams of the transmitter and the receiver $w_T \approx w_R = 1.6 - 2.0$ cm) the scattering diagnostic has a finite wave number acceptance width, $\Delta k = 2/w_R \approx 1.1 \text{ cm}^{-1}$. When the magnetic field line is not exactly perpendicular to the scattering plane, the components of the measured perpendicular wave number spectrum $S(k_\perp)$ are weighted by a factor

$$g(k_\perp) = \exp \left[- \left(\frac{\alpha k_\perp}{\Delta k} \right)^2 \right], \quad (9)$$

whose value increases with k_\perp . In Sec. IV A, we present estimates of wave number spectra both with and without this effect.

IV. DENSITY STEP EXPERIMENT

Initial experiments showed that density profiles in long-pulse (5–20 s) ECH discharges in ATF are generally quite flat, and are unlikely to drive drift-wave instabilities;¹⁸ similar results have been obtained on other stellarator devices.² In order to have a good chance of observing drift-wave instabilities, we explored a number of experimental regimes to develop techniques of producing plasmas in which $dn/d\rho < 0$. The most effective method was found to be an applied density step perturbation, which modified the density profile without drastically altering the temperature profile.

In this paper, we present and analyze fluctuation characteristics for a density step experiment in a currentless ATF plasma sustained by ECH power ($P_{\text{ECH}} = 300 - 400$ kW at 53.2 GHz). The magnetic field in this experiment was $B_0 = 0.95$ T (second harmonic ECH), the chord-average den-

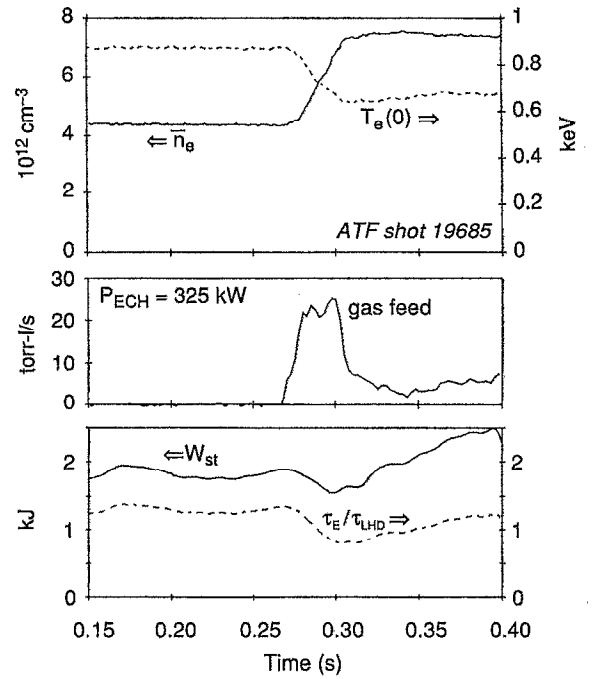


FIG. 3. Time history of the chord-average electron density (\bar{n}_e), central electron temperature $T_e(0)$, gas feed, plasma stored energy (W_{st}), and energy confinement time normalized to that expected for LHD confinement scaling in the density step experiment.

sity varied in the range $\bar{n}_e = (4 - 8) \times 10^{12} \text{ cm}^{-3}$, and the central electron temperature was $T_e(0) = 650 - 900$ eV. Figure 3 shows the temporal evolution of the line-average density \bar{n}_e , plasma stored energy W_{st} , central electron temperature $T_e(0)$, and gyrotron power P_{ECH} during a typical density step. External gas puffing at $t = 0.26$ s leads to an increase of the average density from the lower stationary level ($4.5 \times 10^{12} \text{ cm}^{-3}$) to the higher one ($8 \times 10^{12} \text{ cm}^{-3}$). During the density rise, $T_e(0)$ decreases from about 900 to 650 eV. The plasma stored energy W_{st} shows some decrease during the gas puff, followed by an increase with density. The remarkable feature of this regime is that at the stationary density levels, the density profiles are flat or slightly hollow at normalized radii $\rho \leq 0.85$. During the transition from lower to higher density, the $n_e(\rho)$ profiles become more peaked at radii $\rho \geq 0.65$, as shown in Fig. 4. The onset of the negative density gradient in the confinement region corresponds to the time interval $0.3 < t < 0.35$ s. The electron temperature radial profile remains peaked throughout the density step perturbation (Fig. 4).

The density step also results in a transient change in the energy confinement time relative to that expected for L-mode stellarator discharges. Figure 3 includes a trace of the instantaneous energy confinement time $\tau_E = W_{\text{st}}/P_{\text{ECH}}$ normalized to the confinement time expected for the Large Helical Device (LHD) scaling used in benchmarking L-mode confinement in stellarators:²

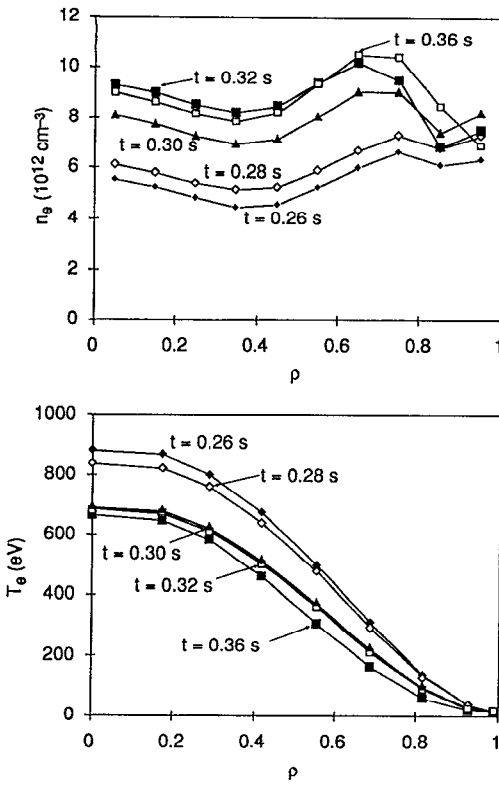


FIG. 4. Evolution of the electron density and temperature profiles during the density step.

$$\tau_E^{\text{LHD}} = 0.17 B_T^{0.84} \left(\frac{\bar{n}_e}{10^{20}} \right)^{0.69} P^{-0.58} R_0^{0.75} a^2 \quad (10)$$

(s, T, m⁻³, MW, m).

During the density step, the normalized confinement time falls from about 1.2 times the LHD confinement time for the initial flat density profile to 0.8 times the LHD value, after which it recovers its original value as the density profile relaxes to a flatter shape. However, the drop in plasma stored energy is comparable to the energy required to ionize and heat the additional gas added during the gas puff.³² Thus, we conclude that, within the limitations of our measurement techniques, no significant change in intrinsic global energy confinement is observed during these profile modification experiments.

A. Wave number spectra of the density fluctuations

During the density step, the amplitudes of the scattering signals change as the plasma profiles change. This change is illustrated in a general way in Fig. 5, which shows the time history of a scattering signal for $k_{\perp} = 7 \text{ cm}^{-1}$ from a scattering volume that extends from $\rho = 0.35$ to $\rho = 0.67$, together with the calculated density gradient at $\rho = 0.65$ – 0.75 . As the density gradient goes negative, the scattering signal rises; it then falls as the gradient returns toward its original value. In this section, we describe the evolution of the wave number spectra measured with scattering during this perturbation ex-

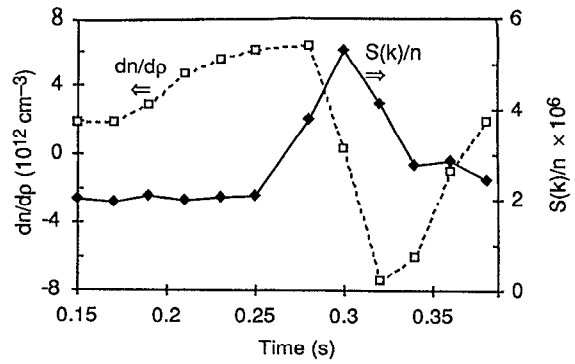


FIG. 5. Time variation of the density gradient at $\rho = 0.65$ – 0.75 and the relative fluctuation level $[S(k = 7 \text{ cm}^{-1})/n \propto (\bar{n}/n)^2]$ at $\rho = 0.35$ – 0.67 during the density step experiment.

periment and also describe the degree of radial localization of the fluctuations that can be discerned with our scattering diagnostic.

The signals used for estimation of the k_{\perp} spectra are chosen so as to avoid contamination of measurements in the plasma core by high levels of edge turbulence. Moreover, the scattering volumes used for the spectral estimates were chosen to be above or below the magnetic minor axis (i.e., at $R \approx 208 \text{ cm}$) to avoid inclusion of the inner–outer asymmetry effect described in Sec. IV D. The wave numbers of the signals used for estimation of the k_{\perp} spectra are presented in Table I, along with the minor radial extent of the corresponding scattering volume (ρ_{\min} and ρ_{\max}) and the number of the microwave receiving channel used. Figure 6 shows the scattering volumes for four of the chords listed in Table I; the volumes for the other chords are similar.

To construct the wave number spectrum, we use data from five different ATF long-pulse discharges with density steps (Fig. 3) whose parameters (ECH power, electron temperature, electron density, and their profiles) were carefully checked to be the same. Figure 7(a) shows the evolution of the k_{\perp} spectra determined in this way during the density step experiment. The spectrum is initially flat, but a large peak appears as the density profile develops a region with negative gradient ($t > 0.28 \text{ s}$). This peak gradually disappears as the density profile flattens after $t = 0.32 \text{ s}$. The maximum intensity of the k_{\perp} spectrum corresponds to $k_{\perp} = 12.4 \text{ cm}^{-1}$ ($k_{\perp} \rho_s \approx 1$). The observation that signals with higher poloidal

TABLE I. Wave numbers, minimum/maximum radii, and channel numbers for scattering volumes used to estimate wave number spectrum.

$k_{\perp}, \text{cm}^{-1}$	ρ_{\min}	ρ_{\max}	Channel
6.6	0.35	0.65	2
7.5	0.47	0.90	3
8.1	0.17	0.61	3
11.5	0.34	0.65	3
12.4	0.49	0.68	2
14.3	0.47	0.81	3
16.6	0.49	0.67	1
18.4	0.48	0.73	2

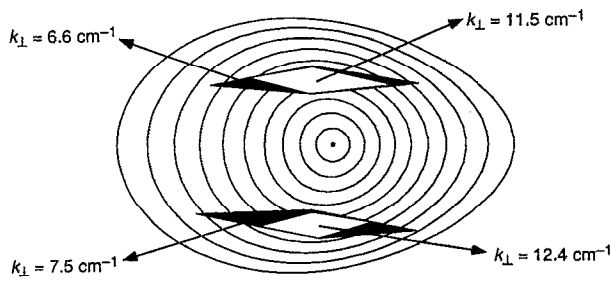


FIG. 6. Locations of the scattering volumes for four of the antenna geometries used for estimates of k_{\perp} spectra. The other scattering geometries listed in Table I are similar.

wave numbers grow faster than those with lower k_{\perp} during the peaking of the density profile is confirmed by examination of the time history of signals with different k_{\perp} , monitored simultaneously during individual discharges. Even if we restrict the choice of the signals by narrowing the range

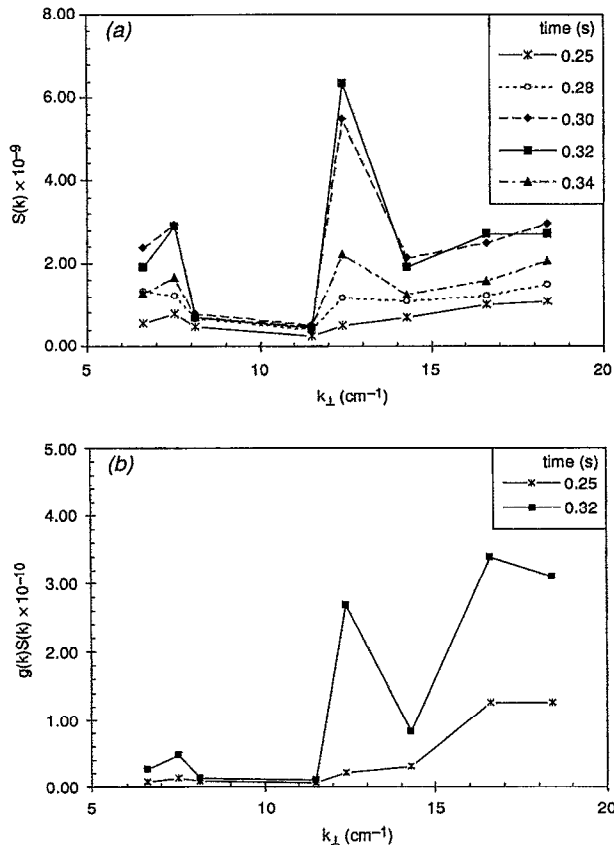


FIG. 7. (a) Evolution of the k_{\perp} spectra of the fluctuations in the plasma confinement region ($0.5 < \rho < 0.85$) during density ramp. (b) Plot of modified k_{\perp} spectra (including the magnetic field pitch effect) at two times during the density step; here $S(k_{\perp})$ has been multiplied by the correction factor $g(k_{\perp})$ from Eq. (9). The field line angles for $\rho=0.6$ in the scattering volumes of Table I were used to compute $g(k_{\perp})$; the increase in the spectrum at high k_{\perp} is probably overestimated because of this conservative assumption.

of the radial expansions of the scattering volume to, for example, $0.65 \leq \rho_{\max} \leq 0.68$, the striking feature of Fig. 7(a)—the growth of the signals with higher k_{\perp} —is still apparent. This result is quite independent of the details of the normalization procedure (each signal is normalized by the number of electrons in the corresponding scattering volume) and the instrument calibration (four out of eight signals are measured with the same antenna—channel 3).

If we include the field line pitch effect on the scattered wave number spectrum^{30,31} by multiplying $S(k_{\perp})$ from Fig. 7(a) by $g(k_{\perp})$ from Eq. (9), the high wave number portion of the spectrum is enhanced, as is shown in Fig. 7(b) for time slices before the density step and at the time of maximum turbulence amplitude. Note that the field line pitch angles used for the calculation of $g(k_{\perp})$ were chosen to correspond to those at $\rho=0.6$ in the scattering volumes listed in Table I and illustrated in Fig. 6, and fall in the range of 5° – 6° . In fact, the portions of the scattering volumes that dominate the measurements may well fall farther out toward the tips of the volumes, where the field line pitch angle is lower [see Fig. 6 and Eq. (8)], and $g(k_{\perp}) \rightarrow 1$, which would cause the “corrected” spectrum to approach more closely the original spectrum shown in Fig. 7(a). A precise answer to this question requires deconvolution of the radial profile of the turbulence amplitude within the scattering volume, which is beyond the scope of our present measurements and analysis. The “corrected” spectrum shown in Fig. 7(b) probably overestimates the enhancement of the spectrum at high wave numbers. In any case, the essential conclusion of the experiment—that high wave number activity rises during the density step—remains the same.

The scattering volumes used to construct the spectra in Fig. 7 were selected to give a good range of wave number coverage and radial resolution just sufficient to avoid pollution by edge turbulence. We can, however, get further supporting information on the radial localization of the fluctuations that grow during the perturbation of the density step by carefully comparing the response of signals from scattering volumes having different radial extents. Figure 8(a) compares two signals with $k_{\perp} \approx 17 \text{ cm}^{-1}$, but with different scattering volumes. In one case, the scattering volume clearly excludes the plasma edge ($\rho_{\max}=0.67$), while in the other it extends all the way to the edge ($\rho_{\max}=0.99$). Both of these scattering volumes include the region where the density gradient changes sign during the density step (see the profiles in Fig. 5). The relative time behavior of the signals is similar—both of them rise and then fall during the density step. The spectral power density for the larger scattering volume, which extends to the edge, is about a factor of 2 larger than that for the smaller volume that excludes the edge; this factor is comparable to the ratio of the two volumes.

The situation is quite different when we compare signals for which one of the scattering volumes excludes the region where the density gradient changes during the perturbation. Figure 8(b) compares the time behavior of two signals having $k_{\perp} \approx 12$ – 13 cm^{-1} . The signal for the scattering volume that extends into the region where the gradient changes sign during the density step again shows the characteristic rise and fall seen in the signals shown in Figs. 5 and 8(a), while

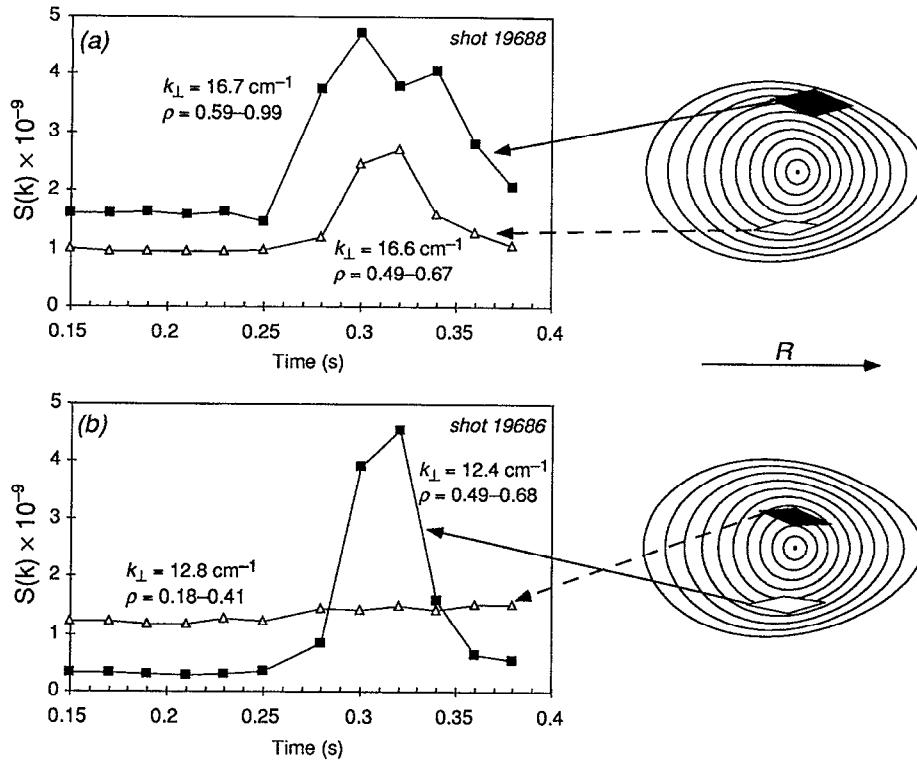


FIG. 8. Time history of the scattering signals during density steps for $k_{\perp} \approx 17 \text{ cm}^{-1}$ and $k_{\perp} \approx 12\text{--}13 \text{ cm}^{-1}$ for the scattering volumes shown: (a) $k_{\perp} = 16.6 \text{ cm}^{-1}$, $\rho = 0.49\text{--}0.67$ (triangles); $k_{\perp} = 16.7 \text{ cm}^{-1}$, $\rho = 0.59\text{--}0.99$ (squares); (b) $k_{\perp} = 12.8 \text{ cm}^{-1}$, $\rho = 0.18\text{--}0.41$ (triangles); $k_{\perp} = 12.4 \text{ cm}^{-1}$, $\rho = 0.49\text{--}0.68$ (squares).

the signal from the scattering volume that extends only to $\rho_{\text{max}} = 0.41$ (thus excluding the region where the gradient changes sign) changes little during the density step.

Similar comparisons for lower wave numbers ($6 \text{ cm}^{-1} < k_{\perp} < 12 \text{ cm}^{-1}$) show the same trends. These results suggest that the rise in fluctuations seen in the scattering signals are associated with the change of gradient in the region $\rho \approx 0.5\text{--}0.85$ and are not due to edge turbulence.

B. Measured density fluctuation levels

We assume that the fluctuations are symmetric with respect to poloidal and radial wave number components, which appears to be at least roughly the case (see Sec. IV D), at least in the center and on the small major radius side of the torus ($R \leq R_0$). This symmetry is used in computing the relative density fluctuation level, as was explained in Sec. III B:

$$\left(\frac{\tilde{n}}{n}\right)^2 \propto \sum_{k_{\perp}} S(k_{\perp}) k_{\perp} \Delta k_{\perp}. \quad (11)$$

The relative level of the density fluctuations in the confinement region of the plasma ($0.5 \leq \rho \leq 0.85$), integrated over the range of wave numbers $6.6 \text{ cm}^{-1} \leq k_{\perp} \leq 18.4 \text{ cm}^{-1}$, is $\tilde{n}/n = 7 \times 10^{-3}$ before the peaking of the density profile and $\tilde{n}/n = 1.4 \times 10^{-2}$ at $t = 0.32 \text{ s}$, when the fluctuation amplitude reaches its maximum value. Note that the value \tilde{n}/n is obtained by summing spectral power densities $S(k_{\perp})$ normalized to the number of electrons in the corresponding scatter-

ing volume. During the density step experiment, when the fluctuations probably increase in only a limited part of the scattering volume (i.e., where the density gradient is negative), only a fraction of the electrons inside the scattering volume contribute to the scattered wave. If this is indeed the case, the local fluctuation level is underestimated.

If we include the field line pitch effect on the measured spectrum [see Eq. (8), Sec. IV A, and Fig. 7], the estimated fluctuation amplitudes are higher: $\tilde{n}/n = 1.7 \times 10^{-2}$ before the peaking of the density profile and $\tilde{n}/n = 3.7 \times 10^{-2}$ at $t = 0.32 \text{ s}$. As discussed previously, our calculation of this effect overestimates the enhancement of the spectrum at high wave number, and thus the inferred turbulence amplitudes are probably too high. A reasonable conclusion is that the two estimates from our scattering data roughly bracket the actual turbulence amplitudes.

Previous measurements of \tilde{n}/n in similar ATF ECH plasmas without the density step were made with the HIBP and with reflectometry.¹⁶ In the radial range covered by the scattering data ($0.5 \leq \rho \leq 0.85$), these experiments yielded $\tilde{n}/n \approx 5 \times 10^{-3}$, which is quite close to the lower estimate of $\tilde{n}/n = 7 \times 10^{-3}$ found in the scattering experiments. This suggests that the wave number range accessible to scattering includes much of the turbulence present in the plasma; it must be noted, however, that all three techniques have gaps in their coverage of the fluctuation wave number spectra. The microwave scattering system used in this study does not yield much usable information on fluctuations with $k_{\perp} \rho_s < 0.5$; as noted in Sec. VI, additional measurements in

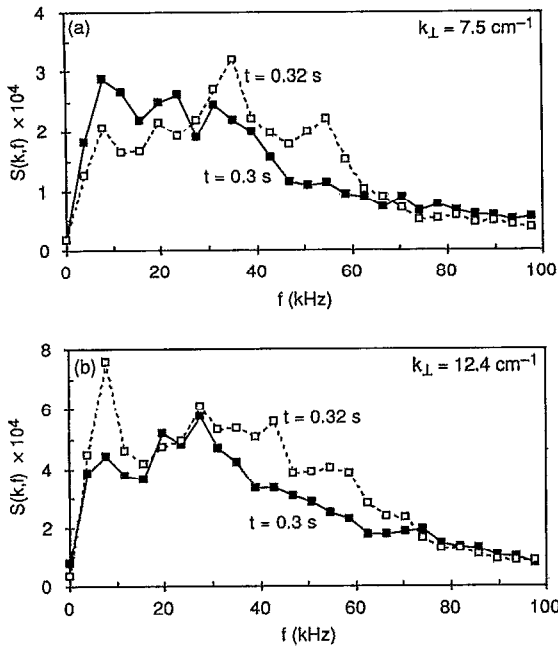


FIG. 9. Frequency spectra of the fluctuations with (a) $k_{\perp} = 7.5 \text{ cm}^{-1}$ and (b) $k_{\perp} = 12.4 \text{ cm}^{-1}$ during the period when $dn/d\rho < 0$ at $\rho \approx 0.7$.

this range are needed to fully document the turbulence in ATF.

C. Frequency spectra of the density fluctuations

The measured turbulence is characterized in the scattering database by both frequency spectra and average frequencies, defined as $f_{av} = \sum f_i S_i / \sum S_i$. The maximum fluctuation spectral amplitude for most plasma conditions occurs in the range $f = 5\text{--}20 \text{ kHz}$, while the average frequency varies between 25 and 50 kHz for the plasma core and between 30 and 90 kHz for the plasma edge. The widths of the frequency spectra are typically $\Delta f/f \approx 0.6$.

Figure 9 shows the frequency spectra observed in the standard magnetic configuration during the density step experiment. The increase in the fluctuation amplitude that accompanies the steepening of the density profile occurs over the entire frequency range. However, when the density gradient is already negative, further steepening of the profile leads to a small but noticeable shift of the frequency spectra toward higher frequencies, as shown in Fig. 9 for the signals with $k_{\perp} = 7.5 \text{ cm}^{-1}$ and $k_{\perp} = 12.4 \text{ cm}^{-1}$. Note that for these scattering geometries, the radial components of the wave numbers are much higher than the poloidal components, i.e., $k_p \gg k_{\theta}$, so that the Doppler shifts caused by bulk poloidal rotation of the plasma (described later in this section) are not important.

The average frequencies of fluctuations with different perpendicular wave numbers are close, so that the difference in average frequency is less than the spectral width. The temporal evolution of the mean frequencies in the density step experiment shows that the behavior of fluctuations with

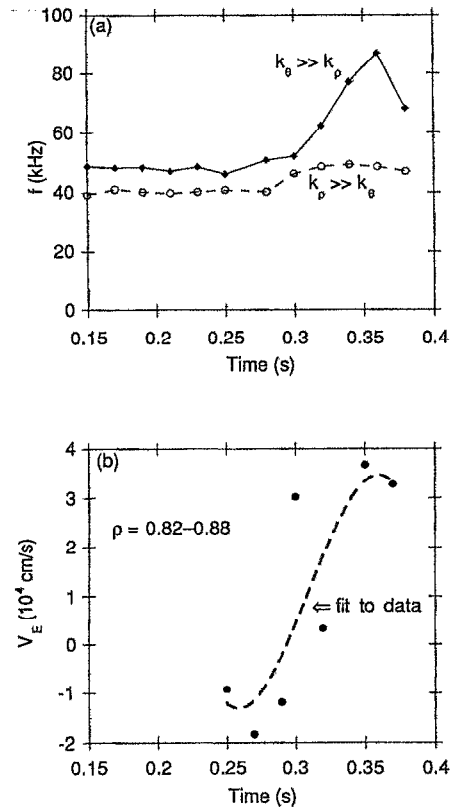


FIG. 10. (a) Evolution of average fluctuation frequency during the density step. The $k_{\theta} \gg k_p$ curve corresponds to the signal with $k_{\theta} = 6.8 \text{ cm}^{-1}$ ($k_{\perp} = 7 \text{ cm}^{-1}$), $R = 182 \text{ cm}$, and $\rho = 0.45\text{--}1$; the $k_p \gg k_{\theta}$ curve corresponds to $k_p = 6.55 \text{ cm}^{-1}$ ($k_{\perp} = 6.8 \text{ cm}^{-1}$), $R = 208 \text{ cm}$, and $\rho = 0.69\text{--}1$. (b) Plasma bulk $\mathbf{E} \times \mathbf{B}$ rotation velocity at $\rho \approx 0.85$ (based on heavy-ion beam probe measurements of the plasma potential profile).

predominantly radial ($k_p \gg k_{\theta}$) wave numbers is different from that of fluctuations with predominantly poloidal ($k_{\theta} \gg k_p$) wave numbers. In comparing calculated frequencies with those obtained from the experimental data, the Doppler

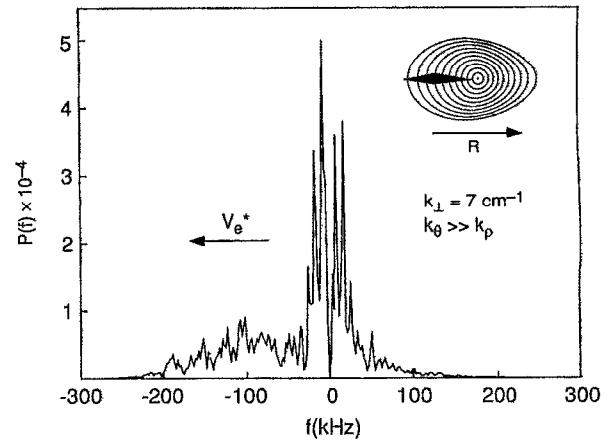


FIG. 11. Dual-homodyne measurement of the fluctuation frequency spectrum. Negative frequencies correspond to the electron diamagnetic direction. Note that because of the geometry, the scattering volume touches the plasma edge (see the inset).

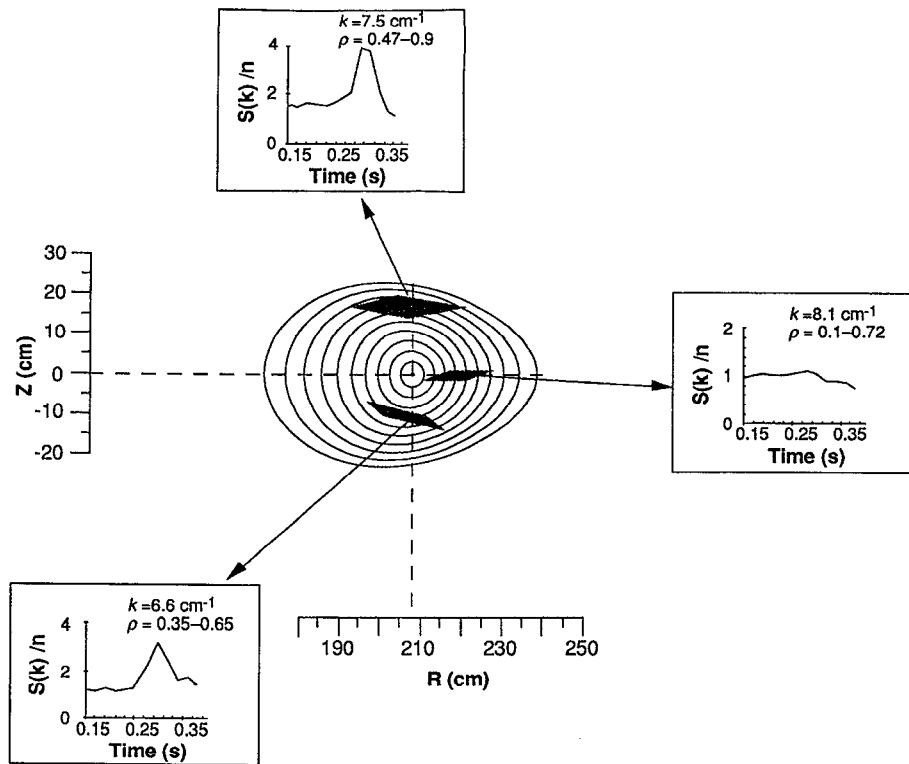


FIG. 12. Spatial asymmetry of the fluctuations in the confinement region (the edge at $\rho=1$ excluded).

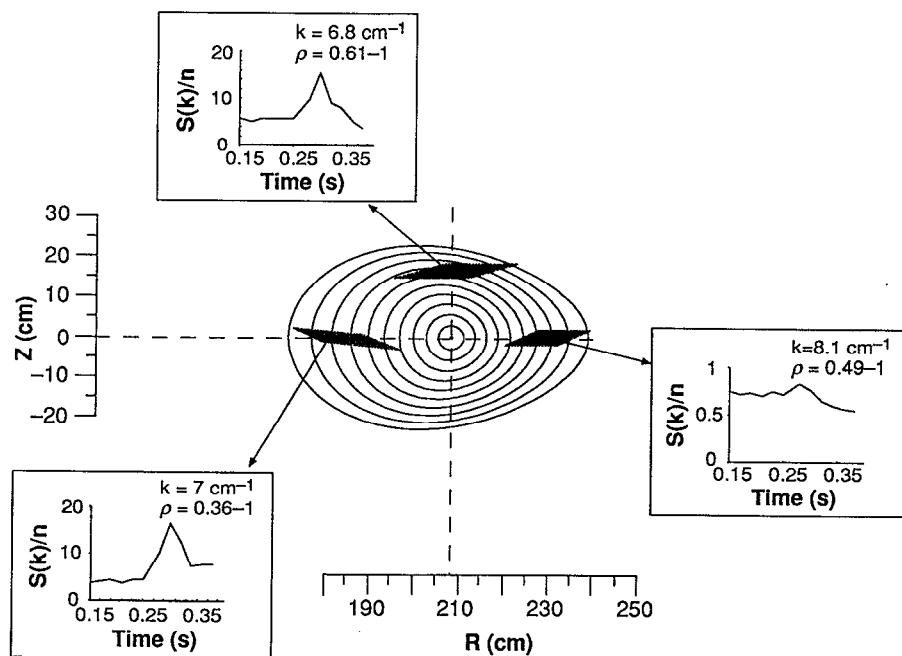


FIG. 13. Spatial asymmetry of the fluctuations in the gradient region (the edge at $\rho=1$ included).

shift caused by the bulk plasma poloidal rotation must be included:

$$\omega_{\text{exp}} = \omega(\mathbf{k}) + k_{\theta} V_{\text{bulk}}, \quad (12)$$

where our notation also includes a wave number dependence (dispersion) for the plasma wave itself. Only waves with significant poloidal wave number components k_{θ} contribute to this frequency shift. When the scattering volume is located above or below the equatorial plane $z=0$, the poloidal wave number component k_{θ} is negligible in comparison with the radial component k_{ρ} , so we can obtain an estimate of $\omega(\mathbf{k})$ without the Doppler shift. The effect of the Doppler shift due to plasma rotation can account for the differences in the temporal evolution of mean frequencies of signals with either mainly poloidal or mainly radial wave number components. As shown in Fig. 10(a), the average frequency of the signal with $k_{\theta} \gg k_{\rho}$ almost doubles during the transition to a higher density level, while the average frequency signal with $k_{\rho} \gg k_{\theta}$ does not change significantly. Both signals may be contaminated by edge turbulence ($\rho=1$); the shear layer at the plasma edge¹² thus contributes to the observed Doppler shift.

If we assume for this experimental comparison that the observed frequency shift is due simply to the $\mathbf{E} \times \mathbf{B}$ poloidal velocity, we consider the relations

$$\begin{aligned} \omega_1 &= \omega_0(\mathbf{k}) + k_{1\theta}(\mathbf{E} \times \mathbf{B})/B^2, \\ \omega_2 &= \omega_0(\mathbf{k}) + k_{2\theta}(\mathbf{E} \times \mathbf{B})/B^2, \end{aligned} \quad (13)$$

where ω_1 and ω_2 are the frequencies of two signals in the laboratory frame of reference, $\omega_0(\mathbf{k})$ is the frequency of the plasma wave, and $k_{1\theta}$, $k_{2\theta}$ are the poloidal wave numbers of the fluctuations. For the frequencies presented in Fig. 10, these equations give a radial electric field $E_r \approx -4$ V/cm, which is comparable with the measured value.¹⁸ Taking into account the Doppler shift, one can deduce an average fluctuation frequency in the plasma frame of reference. For the signals in Fig. 10, this estimate gives $f=40$ kHz. Thus, the bulk plasma rotates with a velocity of about 5×10^4 cm/s in the electron diamagnetic direction. This value is in very good agreement with that deduced from HIBP measurements of the plasma potential profile. Figure 10(b) presents the time history of the $\mathbf{E} \times \mathbf{B}$ rotation velocity computed from the HIBP potential profile measurements at $\rho=0.82-0.88$ in this series of discharges; positive values correspond to rotation in the electron diamagnetic direction. The fluctuations propagate in this direction as well, as is shown by dual-homodyne measurements of the scattering signals having mainly poloidal component wave number components (k_{θ}). As shown in Fig. 11, the frequency spectrum is downshifted with respect to the probe-wave frequency. This corresponds to the electron diamagnetic direction in this scattering geometry. Note that this scattering volume contains an edge contribution because of geometrical constraints like those for the measurements with $k_{\theta} \gg k_{\rho}$ presented in Fig. 10.

D. Spatial asymmetry of the fluctuations

Figures 12 and 13 show the amplitudes of the fluctuations during the density step at different locations in the plasma. The signals chosen here have wave numbers in the

poloidal plane in the range $k_{\perp}=6.6-8.1$ cm⁻¹. The limited spatial resolution does not allow accurate comparison of the local fluctuation intensity as a function of major radius, but qualitative conclusions for the main plasma ($\rho<0.85$) and the periphery ($\rho \approx 1$) can be made. Figure 12 shows the temporal evolution of the scattering signal amplitudes (normalized by the mean density in the scattering volume) $S(k_{\perp})/n \propto [\tilde{n}(k_{\perp})/n]^2$ during the density step. Note that the scattering volumes for these signals do not include the edge region, $\rho \approx 1$. When the density profile develops steep negative gradients, the amplitudes of signals from scattering volumes with $R < R_0$ (both above and below the equatorial plane) are three to four times higher than those of signals from $R > R_0$. Signals from scattering volumes located above ($z > 0$) and below ($z < 0$) the equatorial plane, but at the same major radius, are relatively symmetric in intensity. Comparison of signals that include scattering from the plasma edge reveals even greater inner-outer asymmetry of the intensities along the major radius, as is shown in Fig. 13. The fluctuation levels for $R < R_0$ are much higher in the plasma edge than in the confinement region, but again, signals for $R < R_0$ are much larger than those for $R > R_0$.

V. MAGNETIC CONFIGURATION SCANS

The experimental data presented in Sec. III are for the standard magnetic configuration of ATF. This configuration can be altered by varying the currents flowing in three independent sets of poloidal field coils. This permits variation of the dipole and quadrupole moments of the magnetic configuration.³³ Variation of the dipole moment $\Delta \hat{Q}_{10}$ changes the major radial position of the magnetic axis. Variation in the quadrupole moment $\Delta \hat{Q}_{20}$ changes the (axisymmetric) elongation of the magnetic surfaces. Appropriate choice of the moments permits fine control of magnetic configuration parameters such as rotational transform profile, shear, magnetic well depth, and the fraction of trapped particles that are confined in the vacuum magnetic field.³⁴

We compare relative levels of density fluctuations for the three magnetic configurations shown in Fig. 14(a) for signals with $k_{\perp}=14.3$ cm⁻¹. Although the antenna geometry is the same for the signals that are shown, the spatial resolutions are different because the scattering volume covers different ranges of the plasma radius, depending on the vertical elongation of the magnetic surfaces. The characteristics of the magnetic configurations and the spatial resolutions for $k_{\perp}=14.3$ cm⁻¹ are shown in Table II.

Although the plasma densities in all of the shots used in this comparison are in the range $\bar{n}_e=(4-8) \times 10^{12}$ cm⁻³, the density gradients differ. For example, the discharges in the *V* configuration are characterized by a rather peaked density profile, while in the *U* and *W* configurations, the density profiles vary from flat or hollow to somewhat peaked in the radial range of interest. Since the amplitudes of all of the signals correlate well with the density gradient, we choose for comparison time slices during which the density scale lengths $L_n=n/(dn/dr)$ have comparable values for the different configurations. Figure 14(b) presents the square of the relative fluctuation level [actually $S(k)/n \propto (\tilde{n}/n)^2$] as a function of the confined fraction of trapped particles, f_{ipc} . The

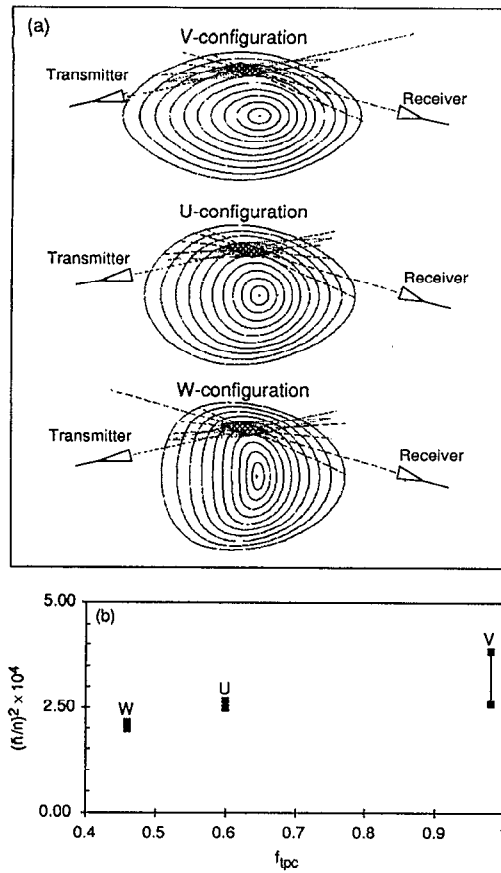


FIG. 14. (a) Vacuum magnetic surfaces and scattering geometry in magnetic configurations with different quadrupole moments (see Table II). (b) Relative fluctuation level $S(k)/n \propto (\tilde{n}/n)^2$ for the configurations illustrated in (a).

fluctuation level is slightly higher for the configurations with higher f_{tpc} : a twofold increase in f_{tpc} produces a 30% increase in the fluctuation level $(S/n)^{1/2}$. A similar tendency is observed during the configuration scan for other fluctuation wave numbers. Nevertheless, there is some uncertainty: in the V configuration, the density scale length L_n is typically shorter than in the other configurations, and this might account for the higher fluctuation level that is observed. Note also that f_{tpc} is calculated for the vacuum magnetic field (i.e., $E_r=0$); in the presence of plasma, the finite radial electric field shifts the loss regions in phase space and can change the effective value of f_{tpc} . Confinement studies of plasmas using configuration scans within single discharges show little variation in energy confinement with f_{tpc} until $f_{tpc} > 0.8$, at which point confinement degrades sharply.³⁴

VI. COMPARISON WITH DRIFT WAVE THEORY

The steepening of the density profile in the confinement region (Fig. 4) creates unique conditions for studying drift wave instabilities, since the scattering diagnostic distinguishes among the plasma edge (where the density gradient is always negative), the confinement region (where the sign of the gradient changes during the density step), and the central region (where the density profile shape changes little). A necessary condition for the DTEM to become unstable is

$$\frac{dT_e}{d\rho} \frac{dn}{d\rho} > 0. \quad (14)$$

Thus, by controlling the sign of the density gradient in the confinement region of the plasma while maintaining $dT_e/d\rho < 0$, one can, in principle, excite drift waves. During the density step, Eq. (14) is satisfied from about $t=0.3$ s to $t=0.35$ s, and a clear correlation of the relative fluctuation level with the sign of the density gradient at $\rho \approx 0.65-0.7$ is observed (Figs. 5 and 8). This observation is important evidence for a drift-wave mechanism as the origin of the fluctuations.

The linear theory of drift waves in stellarators provides a plausible qualitative explanation of some of the fluctuation characteristics observed in the density step experiments on ATF. A collisionality parameter $\nu_e^* = \nu_{eff}/\omega_{be}$ (where ν_{eff} is the effective electron-ion collision rate, which is ν_{ei}/ϵ_t for toroidal trapping and ν_{ei}/ϵ_h for helical trapping, and $\omega_{be} = V_{te}/L_{||}$ is the electron bounce frequency) must be less than one for the DTEM to exist. Electrons trapped in the helical ripples of stellarators have a different ν_e^* than do toroidally trapped electrons, and can drive helical DTEMs.⁹

For typical ATF plasmas, the condition $\nu_e^* < 1$ is easier to satisfy for helically trapped electrons because the connection length of the helical field ripple $L_{||} = 2\pi R/M$ (M is the number of field periods; for ATF, $M=12$) is shorter than the connection length of the toroidal magnetic well $L_{||} = qR$. Figure 15 shows radial profiles of the collisionality parameter ν_{eh}^* and ν_{et}^* computed for the conditions of the density step experiment. For these calculations, an effective ion charge $Z_{eff}=2.5$ (typical for ECH discharges in ATF) was used. In the radial range of interest ($0.5 \leq \rho \leq 0.85$), the condition $\nu_e^* < 1$ is satisfied only for the helically trapped electrons. Toroidally trapped electrons do not enter the collisionless

TABLE II. Parameters for the magnetic configuration scan.

Configuration	Chord length, cm	Quadrupole moment $\Delta\hat{Q}_{20}$	Confined trapped-particle fraction, f_{tpc}	Scattering spatial resolution, $\Delta\rho$ at $\rho=(r/a)$
V	74.4	0.032	0.98	0.55 at $\rho=0.9$
U (standard)	66	0	0.6	0.47 at $\rho=0.81$
W	57.6	-0.035	0.46	0.38 at $\rho=0.64$

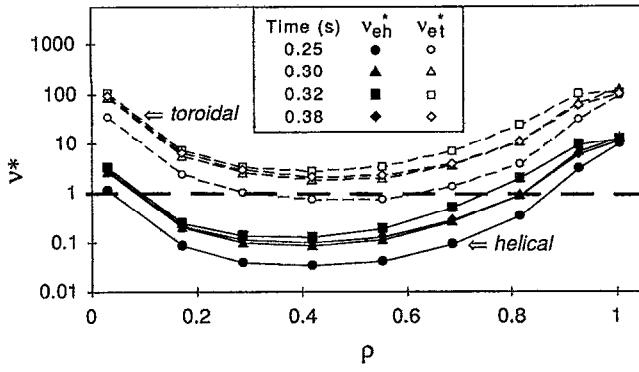


FIG. 15. Radial profiles of the dimensionless collisionality parameters ν_{eh}^* for the helically trapped electrons and ν_{et}^* for the toroidally trapped electrons.

regime (at least when the density gradient is negative in these experiments), and therefore a toroidally induced DTEM is unlikely to occur. Also, when $\nu_{eh}^* < 1$, one can expect the development of the universal or collisionless drift instability,^{35,36} associated with the inverse Landau damping of the wave on the circulating (untrapped) electrons as a dissipation mechanism.

As soon as $\nu_{eh}^* < 1$ and the gradient condition in Eq. (14) is fulfilled, helically trapped electrons can drive the DTEM instability. An existence condition for helical DTEMs establishes a lower bound on the unstable wave numbers:⁹

$$k_{\theta, \text{hel}}^2 \rho_s^2 (1 + 3\delta) > \frac{1}{(3R_0^2/M^2 r L_n^2) - 1}, \quad (15)$$

where the normalized amplitude of the helical stellarator field is given by δ ($=0.32$ for the ATF configuration).

For the parameters of the plasma during the density step, the value of the density scale length L_n plays a critical role in the inequality of Eq. (14). Figure 16 shows a plot of the lowest unstable wave number $k_{\theta, \text{hel}}^{\min}$ of the helically induced DTEM [from Eq. (15)] versus time. Only fluctuations with $k_{\theta, \text{hel}} > 11 \text{ cm}^{-1}$ can become unstable at $t=0.32 \text{ s}$.

The growth rate of the helically induced DTEM is calculated using the expression of Dominguez *et al.*:⁹

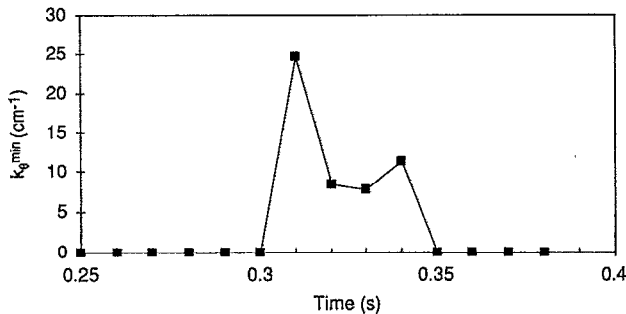


FIG. 16. Minimum wave number of the unstable helical DTEM versus time for the density step experiment (Fig. 3).

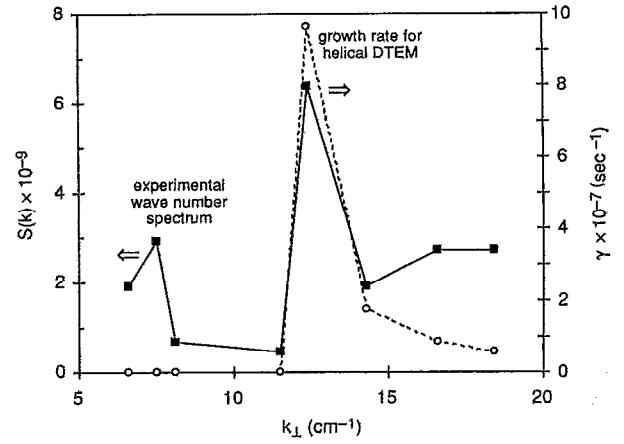


FIG. 17. Experimental k_{\perp} spectrum (squares) and calculated linear growth rates [circles, from Eqs. (13) and (14)] of the helical DTEM for the plasma parameters corresponding to $t=0.32 \text{ s}$ in the density step experiment (Fig. 3).

$$\gamma = 2\sqrt{2} \frac{\omega_e^*}{\nu_{\text{eff}}} f_T \left(\frac{3}{2} \eta_e + 1 - \frac{\omega_0}{\omega_e^*} \right) \frac{M \Delta_{\xi}}{1 + \lambda^2 - \omega_e^*/2\omega_0}, \quad (16)$$

where f_T is the fraction of helically trapped particles, ω_e^* is the electron diamagnetic drift frequency, $\eta_e = L_n/L_{Te}$, $\lambda^2 = k_{\theta}^2 \rho_s^2$.

$$\Delta_{\xi} = \frac{1}{M} \left(\frac{2}{3\delta} \right)^{1/4} \left(\frac{\omega_s}{\lambda \omega_0} \right)^{1/2} \quad (17)$$

represents the localization of the wave along the magnetic field [with the sound frequency $\omega_s = (M/R_0)c_s$], and ω_0 is the frequency of the wave. The results of the calculations of the growth rate [Eq. (16)] and existence condition [Eq. (15)] for the density step experiment at $t=0.32 \text{ s}$ and $\rho=0.7$ are combined in Fig. 17, along with the experimental k_{\perp} spectrum, and demonstrate fairly good agreement of the model calculations with the observed k_{\perp} spectra of the fluctuations. Note that the peak in the k_{\perp} spectrum at $t=0.31 \text{ s}$ (Fig. 16) occurs at $k_{\perp} \rho_s \approx 1$, and is thus at much higher k_{\perp} than the maximum density turbulence amplitude in tokamak experiments, such as the Tokamak Fusion Test Reactor (TFTR).^{5,6}

Analysis of the stability of the collisionless drift mode^{35,36} shows that this branch can be unstable as well during the time interval $t=0.31-0.35 \text{ s}$ at $\rho=0.7$. As with the helical DTEM, the growth rate for the collisionless drift mode is positive and has a maximum at $k_{\theta} > 10 \text{ cm}^{-1}$, but in the wave number range of interest $k_{\perp} = 10-18 \text{ cm}^{-1}$, its growth rate is lower by two to three orders of magnitude than that of the helical DTEM.

Another argument in favor of a DTEM origin for the observed fluctuations is that the universal instability cannot account for the experimentally observed in-out spatial asymmetry of the fluctuations (Figs. 12 and 13). The fluctuation amplitude decreases as the scattering volume is moved outward along the major radius. This observation can be explained within the framework of the theory of the helical DTEM. As illustrated by Dominguez *et al.*, for typical ATF configurations, most of the helically trapped particles should

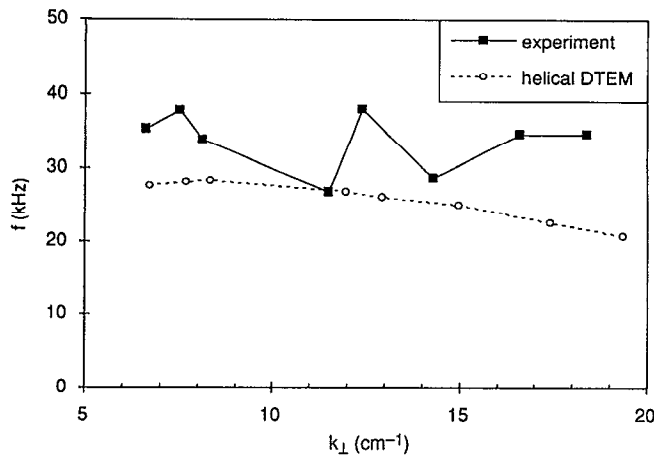


FIG. 18. Theoretical frequencies of the DTEM (circles) and experimentally measured average spectral frequencies for the scattering signals in ATF (solid squares).

be confined inside the magnetic axis ($R < R_0$), owing to the departure of the deeply trapped particle orbits from the flux surfaces.⁹ On the outside ($R > R_0$), the fraction of helically trapped particles that remain confined tends toward zero. Correspondingly, one can expect in-out asymmetry for the helical DTEM. Our observation of the fluctuation asymmetry fits this prediction. [This analysis neglects the effect of the radial electric field that arises to maintain charge neutrality; this electric field can modify the orbits of the trapped particles and change the geometry of the particle trapping regions. We assume that this effect is small in these experiments, where the radial potential difference (estimated from the measurements of E_r) across typical trapped-orbit widths is small compared to the electron thermal energy.]

Some tokamak experiments [see, e.g., early measurements by Mazzucato in the Princeton Large Torus (PLT)³⁷] have exhibited the opposite tendency: the amplitude of the fluctuations in the outer region is considerably higher than that in the inner region. This could be evidence of the influence of toroidally trapped particles in driving the DTEM in a tokamak, where the distribution of the toroidally trapped particles tends to be shifted outward in the torus.

The frequency of the helical DTEM is less than the electron diamagnetic drift frequency ω_e^* ; expressed as ω_e^* times a correction factor, it is given by⁹

$$\omega_0 = \omega_e^* \frac{1 + \delta(M^2 r L_n / 2R_0^2)}{1 + \lambda^2(1 + 3\delta)}. \quad (18)$$

Since the term in δ is small for our experimental parameters, ω_0 is proportional to the density gradient, and the peaking of the density profile should raise this frequency; this is consistent with the experimental observation (Fig. 9). The differences in the frequencies of the fluctuations with different wave numbers k_\perp are within the frequency spectra widths ($\Delta f/f \approx 0.6$). Shown in Fig. 18 are the experimentally observed average spectral frequencies and calculated frequencies of the fluctuations. The $f(k)$ dispersion is calculated from Eq. (18) for the experimental conditions at $t = 0.32$ s.

The experimental data include the average frequency of the spectrum. Only the frequencies of fluctuations with $k_\perp > 6$ cm^{-1} are compared to the calculations because the spatial resolution for lower k_\perp is poor and edge plasma fluctuations can contribute to the scattered waves. The comparatively weak dependence of the fluctuation frequencies comes from the polarization drift effect ($1 + k_\perp^2 \rho_s^2$) in the denominator of Eq. (18).

This stability analysis is in no way comprehensive. Ion Landau damping of both the helically induced DTEM and the collisionless drift wave could play a significant role for these instabilities, since their phase velocities are rather close to the ion thermal velocity: $\omega/k_\parallel \approx 2V_{ti}$. Nonlinear effects, which are not taken into account in this paper, should be considered in connection with the coupling of (and perhaps energy transfer between) higher and lower k_\perp fluctuations and the coupling of modes with primarily poloidal wave numbers to those with primarily radial wave numbers (isotropization).

Although the bulk thermal electrons are not trapped in the magnetic wells of the toroidal ripple ($\nu_{ei}^* > 1$), as is shown in Fig. 15, one could imagine the possibility that the helically driven DTEMs might couple nonlinearly to the toroidal modes. Indeed, the increase in the spectral amplitude at lower wave numbers (Fig. 7) might be explained by the onset of the unstable DTEM driven by toroidally trapped electrons. These modes could be unstable when the condition of Eq. (12) is satisfied and if $\omega_e^* < \nu_{eff}$, as outlined by Kadomtsev and Pogutse.⁸ The latter inequality introduces an upper bound for the wave numbers of the unstable waves. For the parameters of the plasma during the density step at $t = 0.32$ s, it yields $k_\perp < \nu_e/V_e^* = 8$ cm^{-1} (here V_e^* is the electron diamagnetic drift velocity). The experimentally measured k_\perp spectra (Fig. 7) exhibit a gap between the maximum possible wave number of the toroidal DTEM ($k_\perp = 8$ cm^{-1}) and the minimum wave number of the helical DTEM ($k_\perp = 12$ cm^{-1}); it is thus at least plausible that toroidal DTEMs might be present in these experiments. Such an explanation must be regarded as speculative, and requires further exploration.

Experimental measurements of turbulence are often compared with a simple mixing length estimate using the effective radial wave number and gradient length. If we use values from our measurements in ATF during the density step experiments ($k_{\rho,eff} = 12$ cm^{-1} , $L_n = 5$ cm), we obtain

$$\left(\frac{\tilde{n}}{n}\right)_{ml} = \frac{1}{k_{\rho,eff} L_n} \approx 1.7 \times 10^{-2}, \quad (19)$$

which is comparable to the values of \tilde{n}/n estimated from the scattering data (Sec. IV B). This might be taken as additional evidence that the turbulence is large enough to be in the nonlinear regime. However, the radial resolution of our scattering data is not sufficient to permit detailed comparison of our turbulence measurements with the predictions of mixing length calculations (e.g., the response of turbulent amplitudes to local changes in gradient lengths).

VII. DISCUSSION AND CONCLUSIONS

Core plasma density fluctuations in ECH plasmas in the ATF torsatron have been measured using a 2 mm scattering diagnostic. The fluctuation amplitudes are consistent with the presence of marginally stable helical DTEMs. The evidence supporting this conclusion can be summarized briefly.

(i) The increase in fluctuation amplitude correlates with the reversal of the density gradient during the density step.

(ii) The fluctuation amplitudes are asymmetric across the midplane: the amplitudes are much higher on the inside, $R < R_0$, than on the outside, $R > R_0$. This correlates well with expectations for the distribution of the confined helically trapped particles along R in ATF.

(iii) The maximum fluctuation amplitude occurs at relatively high wave numbers, $k_{\perp} \rho_s \sim 1$. This high wave number feature is like that expected for helically induced trapped-electron modes, which are a particular feature of stellarator geometry. An existence condition for these unstable modes establishes a lower bound on the wave number of the waves that is compatible with the experimental observations.

(iv) The frequency spectra of the density fluctuations are generally consistent with expectations for drift waves. The observed density fluctuations propagate in the electron diamagnetic direction. The bulk plasma rotation (diamagnetic plus $\mathbf{E} \times \mathbf{B}$) contributes to the measured frequency shift.

(v) There is some indication from magnetic configuration scans that fluctuation levels increase (albeit modestly) with the confined fraction of trapped particles.

These findings, when combined with the measurements showing transient rearrangement of the density profile, suggest that DTEMs may play a role in constraining the density profile in ECH plasmas in ATF (and perhaps other stellarators as well) to remain flat in regions of high temperature and low collisionality. This hypothesis has also been presented from a theoretical standpoint by Dominguez *et al.*⁹ Interestingly, the profile changes and increase in fluctuations seen in these ATF experiments are not accompanied by a significant change in global energy confinement: τ_E continues to follow L-mode scaling. The apparent insensitivity of the global energy confinement to the appearance of instabilities specifically connected to the three-dimensional helical structure of the stellarator magnetic field is additional evidence that the details of the confining magnetic field are only weakly connected to anomalous energy transport. This observation may have broader implications in the search for the mechanisms governing energy transport in toroidal plasma confinement systems.

Additional experiments would be helpful in clarifying this picture. In a neutral-beam-heated plasma, beam fueling should be able to sustain a density gradient in the high-temperature region of the plasma and fulfill the conditions for excitation of the helical DTEM. A repetition of the scattering measurements for such plasmas could serve as an additional test of the DTEM hypothesis. Also of value would be measurements of the degree of localization of the turbulence in the helical magnetic ripples, temperature fluctuations, and turbulence amplitudes in the low wave number region of the spectrum ($k_{\perp} \rho_s \ll 1$), where significant activity has been observed in tokamaks. These measurements require

additional diagnostics, such as beam emission spectroscopy⁶ or high-resolution correlation reflectometry in the plasma core,⁷ all of which have a higher degree of spatial localization than can be achieved with a microwave scattering diagnostic such as that employed in our experiments on ATF.

Continuing experiments on two devices with magnetic configurations similar to ATF should make it possible to move further into the collisionless regime. The Compact Helical System (CHS) torsatron,³⁸ which is now in operation, has a plasma of comparable size to that of ATF, but at lower toroidal aspect ratio. The Large Helical Device (LHD),³⁹ now under construction, features superconducting magnets with a field of 4 T, a plasma minor radius more than twice that of ATF, and long-pulse heating power.

Comparison of results from devices with significantly different magnetic configurations would also be valuable. In particular, studies of low-collisionality plasmas in the Wendelstein VII-AS stellarator,² whose coils can be powered in different ways so as to vary the rotational transform and/or the effective magnetic mirror ratio of the helical field, could provide essential information on the role of trapped particles in plasma turbulence and transport.

All of these experiments would benefit from theoretical work to aid in planning measurements and interpreting results. Stability calculations in which the effect of the radial electric field is included are important for understanding measurements made in different magnetic configurations. Exploration of the nonlinear behavior of trapped-particle instabilities could help determine the validity of some of the hypotheses used in this study (e.g., coupling of toroidal and helical modes and isotropy of the turbulence).

ACKNOWLEDGMENTS

We are grateful to the members of the ATF group for their many contributions to this work and acknowledge, in particular, G. H. Henkel, M. Holland, L. A. Massengill, T. F. Rayburn, C. R. Schaich, W. Sirmans, and J. L. Yarber for operational support; R. L. Benson and J. A. White for engineering; J. M. Gossett, G. L. King, and T. M. Rayburn for diagnostic measurements; D. C. Giles, D. E. Greenwood, K. L. Kannan, D. R. Overbey, and T. C. Patrick for data handling, and M. B. Nestor for publications assistance. The active support and encouragement of J. Sheffield, W. Fulkeron, and A. W. Trivelpiece of Oak Ridge National Laboratory and L. M. Kovrizhnykh of the General Physics Institute (Moscow) were essential to the execution of this project. Discussions with B. A. Carreras, N. Dominguez, P. K. Mioduszewski, and J. T. Hogan (Oak Ridge National Laboratory), N. Bretz and R. Nazikian (Princeton Plasma Physics Laboratory), and S. M. Hamberger (Australian National University) contributed significantly to the planning of the experiments and the analysis of results.

This work was carried out as part of the U.S.–Russia exchange program in fusion research and was supported in part by the Office of Fusion Energy, U.S. Department of Energy, under Contract No. DE-AC05-84OR21400 with Martin Marietta Energy Systems, Inc.

¹B. A. Carreras, *Plasma Phys. Controlled Fusion* **34**, 1825 (1992).

- ²F. Wagner and U. Stroth, *Plasma Phys. Controlled Fusion* **35**, 1321 (1993).
- ³S. C. Prager, A. K. Sen, and T. C. Marshall, *Phys. Rev. Lett.* **33**, 692 (1974).
- ⁴P. C. Efthimion, D. K. Mansfield, B. C. Stratton, E. Synakowski, A. Bhat-tacharjee, H. Biglari, P. H. Diamond, R. J. Goldston, C. C. Hegna, D. McCune, G. Rewoldt, S. Scott, W. M. Tang, G. Taylor, R. E. Waltz, R. M. Wieland, and M. C. Zarnstorff, *Phys. Rev. Lett.* **66**, 421 (1991).
- ⁵N. L. Bretz, E. Mazzucato, R. Nazikian, S. F. Paul, G. W. Hammett, G. Rewoldt, W. M. Tang, S. D. Scott, E. J. Synakowski, M. C. Zarnstorff, the TFR Group, R. J. Fonck, R. D. Durst, and G. Cosby, in *Plasma Physics and Controlled Nuclear Fusion Research*, 14th International Conference on Plasma Physics and Controlled Nuclear Fusion Research (International Atomic Energy Agency, Vienna, 1993), Vol. 1, p. 551.
- ⁶R. J. Fonck, G. Cosby, R. D. Durst, S. F. Paul, N. Bretz, S. Scott, E. Synakowski, and G. Taylor, *Phys. Rev. Lett.* **70**, 3736 (1993).
- ⁷E. Mazzucato and R. Nazikian, *Phys. Rev. Lett.* **71**, 1840 (1993).
- ⁸B. B. Kadomtsev and O. P. Pogutse, *Nucl. Fusion* **11**, 67 (1971).
- ⁹N. Dominguez, B. A. Carreras, V. E. Lynch, and P. H. Diamond, *Phys. Fluids B* **4**, 2906 (1992).
- ¹⁰J. F. Lyon, B. A. Carreras, K. K. Chiple, M. J. Cole, J. H. Harris, T. C. Jernigan, R. L. Johnson, V. E. Lynch, B. E. Nelson, J. A. Rome, J. Sheffield, and P. B. Thompson, *Fusion Technol.* **10**, 179 (1986).
- ¹¹J. H. Harris, M. Murakami, B. A. Carreras, J. D. Bell, T. S. Bigelow, L. A. Charlton, N. Dominguez, J. L. Dunlap, J. C. Glowienka, L. D. Horton, H. C. Howe, R. C. Isler, H. Kaneko, R. R. Kindsfater, J. N. Leboeuf, V. E. Lynch, M. M. Menon, R. N. Morris, G. H. Neilson, V. K. Paré, D. A. Rasmussen, J. B. Wilgen, and W. R. Wing, *Phys. Rev. Lett.* **63**, 1249 (1989).
- ¹²C. Hidalgo, J. H. Harris, T. Uckan, J. D. Bell, B. A. Carreras, J. L. Dunlap, G. R. Dyer, C. P. Ritz, A. J. Wootton, M. A. Meier, T. L. Rhodes, and K. Carter, *Nucl. Fusion* **31**, 1471 (1991).
- ¹³T. Uckan, C. Hidalgo, J. D. Bell, J. H. Harris, J. L. Dunlap, G. R. Dyer, P. K. Mioduszewski, J. B. Wilgen, C. P. Ritz, A. J. Wootton, T. L. Rhodes, and K. Carter, *J. Nucl. Mater.* **176-177**, 693 (1990).
- ¹⁴J. J. Zielinski, S. C. Aceto, K. A. Connor, J. F. Lewis, J. C. Glowienka, G. H. Henkel, D. T. Fehling, W. R. DeVan, K. D. St. Onge, D. K. Lee, and A. Carnevali, *Rev. Sci. Instrum.* **61**, 2961 (1990).
- ¹⁵G. R. Hanson, J. B. Wilgen, E. Anabitarte, J. D. Bell, J. H. Harris, J. L. Dunlap, and C. E. Thomas, *Rev. Sci. Instrum.* **61**, 3049 (1990).
- ¹⁶G. R. Hanson, J. H. Harris, J. B. Wilgen, C. E. Thomas, S. C. Aceto, L. R. Baylor, J. D. Bell, B. Brañas, J. L. Dunlap, A. C. England, C. Hidalgo, M. Murakami, D. Rasmussen, J. Sanchez, J. G. Schwelberger, T. Uckan, and J. Zielinski, *Nucl. Fusion* **32**, 1593 (1992).
- ¹⁷M. Murakami, T. S. Bigelow, R. C. Goldfinger, J. B. Wilgen, L. R. Baylor, D. A. Rasmussen, A. C. England, S. C. Aceto, F. W. Baity, D. B. Batchelor, G. L. Bell, J. D. Bell, B. A. Carreras, R. J. Colchin, E. C. Crume, N. Dominguez, R. A. Dory, J. L. Dunlap, G. R. Dyer, R. H. Fowler, R. F. Gandy, J. C. Glowienka, R. H. Goulding, G. R. Hanson, J. H. Harris, S. Hiroe, D. J. Hoffman, L. D. Horton, H. C. Howe, D. P. Hutchinson, R. C. Isler, T. C. Jernigan, H. Kaneko, S. Kubo, M. Kwon, R. A. Langley, J. G. Leboeuf, D. K. Lee, K. M. Likin, J. F. Lyon, C. H. Ma, S. Morita, M. Ochando, H. Okada, S. F. Paul, A. L. Qualls, J. A. Rome, A. V. Sapozhnikov, K. A. Sarksyan, M. Sato, J. G. Schwelberger, M. G. Shats, T. D. Shepard, J. E. Simpkins, C. E. Thomas, J. S. Tolliver, T. Uckan, K. L. Vander Sluis, M. R. Wade, W. R. Wing, and J. J. Zielinski, in *Radio Frequency Power in Plasmas*, AIP Conf. Proc. 244, Charleston, 1991 (American Institute of Physics, New York, 1992), Vol. 1, p. 3.
- ¹⁸R. C. Isler, S. C. Aceto, L. R. Baylor, T. S. Bigelow, G. L. Bell, J. D. Bell, T. S. Bigelow, B. A. Carreras, R. J. Colchin, E. C. Crume, N. Dominguez, R. A. Dory, J. L. Dunlap, G. R. Dyer, A. C. England, R. F. Gandy, J. C. Glowienka, G. R. Hanson, J. H. Harris, S. Hiroe, L. D. Horton, T. C. Jernigan, H. Ji, R. A. Langley, D. K. Lee, K. M. Likin, J. F. Lyon, C. H. Ma, S. Morimoto, M. Murakami, H. Okada, A. L. Qualls, D. A. Rasmus-sen, J. A. Rome, M. Sato, J. G. Schwelberger, M. G. Shats, J. E. Simpkins, C. E. Thomas, T. Uckan, M. R. Wade, J. B. Wilgen, W. R. Wing, H. Yamada, and J. Zielinski, *Phys. Fluids B* **4**, 2104 (1992).
- ¹⁹M. Murakami, B. A. Carreras, L. R. Baylor, G. L. Bell, T. S. Bigelow, J. C. Glowienka, H. C. Howe, V. E. Lynch, C. H. Ma, D. A. Rasmussen, J. S. Tolliver, M. R. Wade, J. B. Wilgen, and W. R. Wing, *Phys. Rev. Lett.* **66**, 707 (1991).
- ²⁰O. Asada, A. Inoue, and T. Tsukishima, *Rev. Sci. Instrum.* **51**, 1308 (1980).
- ²¹J. D. Bell, J. H. Harris, J. L. Dunlap, N. A. Crocker, and V. K. Paré, *Rev. Sci. Instrum.* **64**, 2428 (1993).
- ²²C. H. Ma, L. R. Baylor, D. P. Hutchinson, M. Murakami, and J. B. Wilgen, *Rev. Sci. Instrum.* **63**, 4981 (1992).
- ²³G. L. Bell, R. F. Gandy, and J. B. Wilgen, *Nucl. Fusion* **33**, 875 (1993).
- ²⁴R. E. Slusher and C. M. Surko, *Phys. Fluids* **23**, 472 (1980).
- ²⁵R. C. Goldfinger and D. B. Batchelor, *Nucl. Fusion* **27**, 31 (1987).
- ²⁶S. P. Hirshman, W. I. van Rij, and P. Merkel, *Comput. Phys. Commun.* **43**, 143 (1986).
- ²⁷N. Bretz, R. Nazikian, W. Bergin, M. Diesso, J. Felt, and M. McCarthy, *Rev. Sci. Instrum.* **61**, 3031 (1990).
- ²⁸Équipe TFR, *Plasma Phys.* **25**, 641 (1983).
- ²⁹B. A. Carreras, G. Grieger, J. H. Harris, J. L. Johnson, J. F. Lyon, O. Motojima, F. Rau, H. Renner, J. A. Rome, K. Uo, M. Wakatani, and H. Wobig, *Nucl. Fusion* **28**, 1613 (1988).
- ³⁰A. Truc, A. Quéméneur, P. Hennequin, D. Grésillon, F. Gervais, C. Lavi-ron, J. Olivain, S. K. Saha, and P. Devynck, *Rev. Sci. Instrum.* **63**, 3716 (1992).
- ³¹E. Holzauer, G. Dodel, and the ASDEX Team, *Rev. Sci. Instrum.* **61**, 2817 (1990).
- ³²D. Heifetz, in *Physics of Plasma-Wall Interactions in Controlled Fusion*, edited by D. Post and R. Behrisch (Plenum, New York, 1986), p. 695.
- ³³G. H. Neilson and J. H. Harris, *Nucl. Fusion* **27**, 711 (1987).
- ³⁴J. B. Wilgen, M. Murakami, J. H. Harris, T. S. Bigelow, R. A. Dory, B. A. Carreras, S. C. Aceto, D. B. Batchelor, L. R. Baylor, G. L. Bell, J. D. Bell, R. J. Colchin, E. C. Crume, N. Dominguez, J. L. Dunlap, G. R. Dyer, A. C. England, R. F. Gandy, J. C. Glowienka, R. C. Goldfinger, R. H. Goulding, G. R. Hanson, C. Hidalgo, S. Hiroe, S. P. Hirshman, L. D. Horton, H. C. Howe, D. P. Hutchinson, R. C. Isler, T. C. Jernigan, H. Ji, H. Kaneko, L. M. Kovrizhnykh, M. Kwon, R. A. Langley, D. K. Lee, K. M. Likin, J. F. Lyon, C. H. Ma, P. K. Mioduszewski, O. Motojima, H. Okada, S. Paul, A. L. Qualls, D. A. Rasmussen, R. K. Richards, J. A. Rome, M. J. Saltmarsh, K. A. Sarksyan, M. Sato, J. G. Schwelberger, K. C. Shaing, M. G. Shats, T. D. Shepard, J. E. Simpkins, C. E. Thomas, T. Uckan, K. L. Vander Sluis, M. R. Wade, W. R. Wing, H. Yamada, and J. J. Zielinski, *Phys. Fluids B* **5**, 2513 (1993).
- ³⁵C. Z. Cheng and H. Okuda, *Nucl. Fusion* **18**, 587 (1978).
- ³⁶B. B. Kadomtsev, *Plasma Turbulence* (Academic, New York, 1965).
- ³⁷E. Mazzucato, *Phys. Fluids* **21**, 1063 (1978).
- ³⁸H. Yamada, S. Morita, K. Ida, S. Okamura, H. Iguchi, S. Sakakibar, K. Nishimura, R. Akiyama, H. Arimoto, M. Fujiwara, K. Hanatani, S. P. Hirshman, K. Ichiguchi, H. Idei, O. Kaneko, T. Kawamoto, S. Kubo, D. K. Lee, K. Matsuoka, O. Motojima, T. Ozaki, V. D. Pustovitov, A. Sagara, H. Sanuki, T. Shoji, C. Takahashi, Y. Takeiri, Y. Takita, S. Tanahashi, J. Todoroki, K. Toi, K. Tsumori, M. Ueda, and I. Yamada, in Ref. 5, Vol. 2, p. 493.
- ³⁹O. Motojima, K. Akaishi, M. Asao, K. Fujii, J. Fujita, T. Hino, Y. Hamada, H. Kaneko, S. Kitagawa, Y. Kubota, T. Kuroda, T. Mito, S. Morimoto, N. Noda, Y. Ogawa, I. Ohtake, N. Ohya, A. Sagara, T. Satow, K. Takahata, M. Takeo, S. Tanahashii, T. Tsuzuki, S. Yamada, K. Yamamoto, K. Yamazaki, N. Yanagi, H. Yonezu, M. Fujiwara, A. Iiyoshi, and the LHD Design Group, in *Plasma Physics and Controlled Nuclear Fusion Research*, 13th International Conference on Plasma Physics and Controlled Nuclear Fusion Research (International Atomic Energy Agency, Vienna, 1991), Vol. 3, p. 513.